



Journal of Applied and Computational Mechanics



Research Paper

Electrochemical and Mechanical Properties of Ni/g-C₃N₄ Nanocomposite Coatings with Enhanced Corrosion Protective Properties: A Case Study for Modeling the Corrosion Resistance by ANN and ANFIS Models

Alireza Zarezadeh¹, Mohammad Reza Shishesaz², Mehdi Ravanavard¹, Moslem Ghobadi²,
Farzaneh Zareipour³, Mohammad Mahdavian³

¹ Department of Safety Engineering, Abadan Faculty of Petroleum Engineering, Petroleum University of Technology, Abadan, Iran

² Department of Inspection Engineering, Abadan Faculty of petroleum engineering, Petroleum case study University of Technology, Abadan, Iran

³ Surface Coatings and Corrosion Department, Institute for Color Science and Technology, P.O. Box 16765-654, Tehran, Iran

Received August 31 2021; Revised November 29 2021; Accepted for publication December 14 2021.

Corresponding author: M.R. Shishesaz (shishesaz@put.ac.ir)

© 2022 Published by Shahid Chamran University of Ahvaz

Abstract. This work investigates the effect of electrolysis bath parameters on the corrosion, micro-hardness, and wear behavior of Ni coatings. The characterization of synthesized Graphitic carbon nitride (g-C₃N₄) was done by Fourier transform infrared, Raman spectroscopy, and transmission electron microscope. The surface morphology of coated samples with various amounts of current density was studied by scanning electron microscopy and energy-dispersive X-ray spectroscopy. The corrosion prevention effect of Ni/g-C₃N₄ nanocomposite coatings was investigated by EIS and polarization techniques. The experimental outcome demonstrates that an electrolysis bath of 0.3 g/L g-C₃N₄ and 0.1 A.cm⁻² presents a Ni coating with the highest corrosion protection, wear resistance, and microhardness. The corrosion current densities of Ni/g-C₃N₄ coatings obtained by electrochemical tests were used for training two machine learning techniques (Artificial neural network (ANN) and adaptive neuro-fuzzy inference system (ANFIS)) based on current density, g-C₃N₄ concentration, and plating time as an input. Various statistical criteria showed that the ANFIS model (R²= 0.99) could forecast corrosion current density more accurately than ANN with R²= 0.91. Finally, due to the robust performance of ANFIS in modeling the corrosion behavior of Ni/g-C₃N₄ nanocomposite coating, the effect of each parameter was studied.

Keywords: Ni nanocomposite coating; Electrolysis parameter; Electrodeposition; g-C₃N₄; Modeling.

1. Introduction

To extend the lifetime of engineering materials that are subjected to corrosion and wear, surface coatings can be used [1]. Coatings operate as a barrier between the environment and the steel surface. To develop a surface coating of bulk materials, various techniques may utilize. Among several coatings processing, the electrodeposition process is known as the most reliable, cost-effective, and practical surface engineering technique [2]. In the last few years, to improve corrosion resistance, wear, and hardness properties nickel has been extensively used for developing metal-matrix composite structures with various nanoparticles [3]. The electrodeposition process can efficiently coat complex shapes and provide uniform coating thickness. During electrodeposition, insoluble particles are suspended in the electroplating solution and stick to the forming deposit making up the second phase particles. Microcracks are reduced, and the coatings' mechanical behavior is improved when second phase particles are present in the Ni matrix [4].

According to the literature, several studies focused on the Ni electrodeposited composites coating containing SiC [5], Al₂O₃ [6], TiO₂ [7], graphene [8], CeO₂ [9], etc. During the electrodeposition process, the concentration of nanomaterials and electrodeposition parameters (such as deposition duration and current density), significantly affect the electrochemical, physical, microstructure, and mechanical properties of nanocomposite coatings [45-49].

Due to the high nitrogen content of g-C₃N₄ and its layered two-dimensional structure it may have more active reaction sites compared to other N-carbon compounds. Also, due to the nature of the lamellar structure, g-C₃N₄ is frequently well-crystallized, which promotes charge transfer [10]. It has been known for suitable hardness resistance and excellent chemical and thermal stability [13], excellent biocompatibility, biological activity, and corrosion resistance [14]. There are a few reports on the impact of using g-C₃N₄ in the coatings. Fayyad et al. evaluated the impact of C₃N₄ nanoparticles on the electrochemical and mechanical resistance of NiP coatings. First, the optimum value for each electrolysis parameter, as pH, plating time, and surfactant types,



were investigated; then, the optimal concentration of g-C₃N₄ nanoparticles was determined. As a result, they were able to demonstrate that C₃N₄ had a remarkable effect on the corrosion behavior and micro-hardness of the NiP electrodeposition coating [13]. Recently, some researchers evaluated the impact of g-C₃N₄ on the tribological and corrosion behavior of epoxy coatings. It was found that using g-C₃N₄ into the mentioned coatings improves the corrosion and mechanical properties [15-18].

Nowadays, many researchers utilize intelligent reasoning systems to achieve significant improvement in products' quality because of their capability in prioritization, optimization, planning, and forecasting [19]. Application of machine learning tools such as artificial neural networks (ANN) and adaptive neuro-fuzzy inference systems (ANFIS) have recently garnered considerable attention because of their vast capabilities and flexibility of use as compared to other traditional modeling methods [20-22]. ANN is a famous mathematical simulator that is inspired by the structure of the human brain. They have been ordered to have a capacity to accomplish like a human, by instructive data and learning activity [23]. It can learn the linear and nonlinear relevance between different variables from a dataset. In addition, this method is able to simulate various processes without the full realization of mathematical equations and can handle complicated engineering problems [24]. ANFIS is a hybrid universal tool that was firstly introduced by Jang in 1993 [38]. The capabilities of fuzzy logic systems were combined with ANN learning abilities in the ANFIS algorithm [25]. ANFIS assisted in modeling the experimental datasets by converting logical statements to mathematical relations [26]. Based on the learning ability, ANFIS produces a group of rules due to the relation of input-output pairs in a dataset and specifies the best membership functions [24].

ANN was used by Youjun Xu et al. to model the corrosion resistance of Ni-SiC composite coatings produced by ultrasonic electrodeposition and found that constructed model can forecast the corrosion behavior of composite coatings [27]. Hongyu Gan et al. evaluated the ability of three ANN models to simulate the current efficiency and glossiness of silver film which was applied by electrodeposition technique. The results displayed that, when there are enough samples, an extreme learning machine (ELM) is a great choice because it can produce higher accuracy and move faster than conventional ANN models [28]. Xinchun Zhuang et al. utilized several ANN models to forecast the wear properties of Ni-TiN coatings applied by pulse electrodeposition. The outcomes indicated that the application of the ANN model is a promising approach to study the wear behavior of Ni-TiN nanocomposite coatings [29].

In the present article, Ni/g-C₃N₄ nanocomposite coating was applied on the low carbon steel substrate, and the corrosion properties, wear resistance, and microhardness was evaluated according to the value of current density and g-C₃N₄ content. Raman, transmission electron microscopy (TEM), and Fourier transform infrared spectroscopy (FT-IR) was employed to investigate the characterization of the g-C₃N₄ nanoparticles. Characterization of nanocomposite coatings was implemented based on surface morphology using scanning electron microscopy (SEM) and energy-dispersive X-ray spectroscopy (EDS). The corrosion properties examination was done by polarization test and electrochemical impedance spectroscopy (EIS) technique. Moreover, the comparison between pure Ni coating and composite coatings with different amounts of g-C₃N₄ in the microhardness, friction, and wear behavior were comparatively studied. Finally, based on the experimental results, two machine learning tools (ANN and ANFIS methods) were developed to model the effective electrodeposition variables, including current density, g-C₃N₄ particles content, and plating time on the corrosion behavior of the coatings.

2. Materials and Methods

2.1 Materials

NiCl₂.6H₂O (≥ 99%), NiSO₄.6H₂O (99%), and melamine (C₃H₆N₆, 99%) which was used as a precursor of g-C₃N₄, were provided from Merck without further purification. Polyvinylpyrrolidone (PVP), HCl (10%), and acetone were procured from Aldrich Co. The low carbon steel panels (98.3% Fe, 0.14% C, 0.9% Mn, 0.035% P, 0.04% S, 0.4% Si and 0.2% Cu) used as substrates were prepared from Mobarakeh steel Co. (Iran).

2.2 Preparation of Ni/ g-C₃N₄ composites

Graphitic carbon nitride (g-C₃N₄) was synthesized, as reported previously [30, 31]. After heating 15 g of melamine to 550°C for 240 minutes (at a rate of 20 °C/min), g-C₃N₄ nanosheets powder with the fine yellowish apparent was achieved after cooling to room temperature. The direct current electrodeposition process was selected to prepare Ni/g-C₃N₄ nanocomposite coatings. The substrate was polished with 120, 220, 320, 400, 600, 800, 1000, and 1200 grit emery papers, then ultrasonically degreasing in acetone for 10 min and finally etched in HCl for 30 s. Afterward, distilled water was used to wash the substrate surface and immediately immersed in the electrolyte bath solution. In this study, to find the optimum current density, a Ni/g-C₃N₄ electrodeposition bath with a specified amount of g-C₃N₄ concentration (0.5 g/l) was performed at various current densities (0.02, 0.05, 0.1, and 0.2 A/cm²). The steel substrate as cathode and Ni plate as anode vertically were placed in a 250 ml bath. In order to obtain a smoother and more homogeneous coating, PVP has been added to the solution as a surfactant.

The bath compositions and electrodeposition conditions are mentioned in Table 1. To avoid agglomeration, the bath containing g-C₃N₄ was stirred by magnetic stirrer under 400 rpm for 1 h, then solution bath was ultra-sonicated for a duration of 1 h to disperse nanoparticles uniformly (1 W/mL at 24 kHz). During the plating process, a magnetic stirrer was also employed at 400 rpm. After finding the best suitable current density, different electrodeposition solutions with various concentrations of g-C₃N₄ (0.3, 0.9, and 1.8 g/L) were prepared to construct Ni/g-C₃N₄ nanocomposite coating with optimum conditions.

2.3 Characterization

Raman spectroscopy and FT-IR analysis were used for the characterization of g-C₃N₄ nanosheets. Raman spectra of g-C₃N₄ nanosheets were determined employing a confocal Raman (Horiba Xplora plus, France) (532 nm for wavelength incident laser light). The FT-IR analysis was carried out by Perkin Elmer FTIR Spectrum One within the wavenumber range of 500–4000 cm⁻¹. The morphological attributes of g-C₃N₄ nanosheets were identified by transmission electron microscopy (TEM, JEM-2100; Jeol; Japan). To evaluate the surface morphology and elemental analysis of the Ni/g-C₃N₄ coatings, FE-SEM, EDX, and elemental mapping of the coated samples were done by an instrument model MIRA3 TESCAN. In order to investigate the crystal structure and phase analysis of the deposited coatings an X-ray diffraction XRD instrument (model Philips Xpert MPD X-ray diffraction) was utilized. The start and end angles for continuous scanning were 10° and 80°, respectively.

Table 1. Composition and condition of electrodeposition bath of Ni/g-C₃N₄

Compositions	Value (g.L ⁻¹)	Parameters	Value
NiSO ₄ .6H ₂ O	220	Time (min)	45
NiCl ₂ .6H ₂ O	40	pH	4
PVP	0.05	Temperature (°C)	60
Stirring rate (rpm)	400	Electrode distance (mm)	30



2.4 Electrochemical corrosion studies

The potentiodynamic polarization (Tafel analysis) and electrochemical impedance spectroscopy (EIS) techniques were adopted to evaluate the corrosion resistance of the coatings. The electrochemical tests were performed via IVIUM potentiostat-galvanostat device utilizing a flat electrochemical cell containing three entrances for a conventional three-electrode assembly where the coatings material, saturated calomel electrode (SCE), and pure Pt rod were employed as the working, reference, and counter electrodes, respectively. The tests were done in a 3.5 wt% NaCl solution and ambient temperature. The electrochemical measurement tests were arranged in a non-stirred state while the exposed area of all materials was fixed to 1 cm². The frequency ranges from 100 kHz to 10 mHz with imposed AC amplitude of 10 mV was utilized for EIS experiments. In this test, the extraction process of the EIS data was always initiated after the OCP became stable. For Tafel analysis, the opted potential range was from -1.2V to +0.8V with 1 mV/s scanning rate considering OCP, which was applied to procure the cathodic and anodic curves. To warrant the reproducibility of the extracted data and provide a precise indication of the corrosion rate, whole experiments were conducted at least three times. Zview3.1 software was employed to fit the EIS results.

2.5 Wear test

Wear resistance for samples with different g-C₃N₄ concentration were evaluated by pin-on-disc tribometer under dry condition and 25 °C. For this purpose, AISI 52100-5 mm diameter pin and average hardness of 46 HRC was utilized. Rotation speed was fixed at 60 rpm, applied load was set at 5 N, and sliding distance was 200 m during the test. After the wear tests, SEM was used to study the worn surface morphology. All samples were weighed before and after the wear test when the wear debris was removed.

2.6 The microhardness measurements

The microhardness of Ni/g-C₃N₄ nanocomposite coating was obtained by Vickers microhardness tester. The load of 200 g was inserted on the composite coatings surface for 10 seconds. The average value of 3 separate locations on each coating surface was reported.

2.7 Machine learning approaches

The influence of electrolysis bath parameters on the corrosion behavior of Ni/g-C₃N₄ nanocomposite coatings was evaluated utilizing two machine learning methods. A schematic configuration to simulate the corrosion resistance of Ni/g-C₃N₄ nanocomposite coatings based on experimental analysis was presented in Fig. 1. Based on experimental datasets, the electrolysis bath parameters were set as inputs, and the corrosion current densities were selected as the output. Afterward, two models were trained, and the accuracy of each model was examined through various error criteria. Finally, the most suitable and accurate model was proposed for modeling the corrosion current density of Ni/g-C₃N₄ nanocomposite coatings. The accuracy of constructed models was measured by several statistical errors, like MAE which was calculated according to Eq. (1):

$$MAE = \frac{1}{N} \sum_{i=1}^n |t - O| \quad (1)$$

and for calculating the mean-square error (MSE) we can use the following relation:

$$MSE = \frac{1}{N} \sum_{i=1}^n (t - O)^2 \quad (2)$$

In these equations, t is experiment data, n is the number of data for training, and O is predicted data. Also, the coefficient of determination (R^2) was calculated according to Eq. (3):

$$R^2 = 1 - \frac{\sum_{i=1}^{n-1} (t - O)^2}{\sum_{i=1}^{n-1} (t - m)^2} \quad (3)$$

where, m represents the average of the test dataset values. If a model resulted in a lower value of MAE and RMSE, so the model has a suitable accuracy. For the case of R^2 value, the model which results closer to unity represents a better ability for modeling [32].

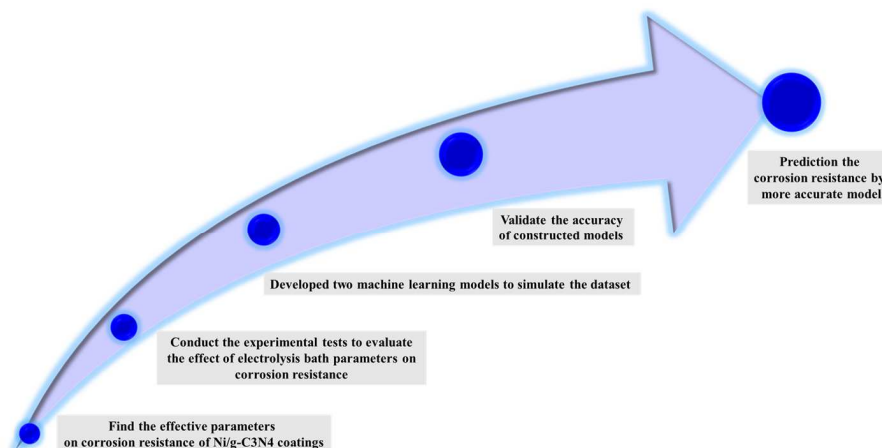


Fig. 1. Schematic configuration to simulate the corrosion resistance of Ni/g-C₃N₄ nanocomposite coatings based on experimental analysis.



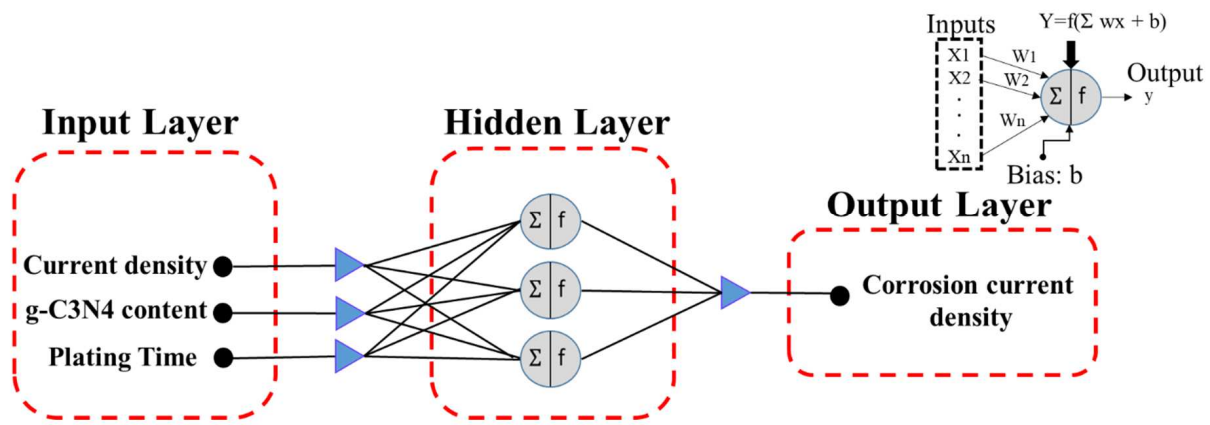


Fig. 2. The structure for the ANN model utilized for modeling the corrosion current density of Ni/g-C₃N₄ nanocomposite coatings.

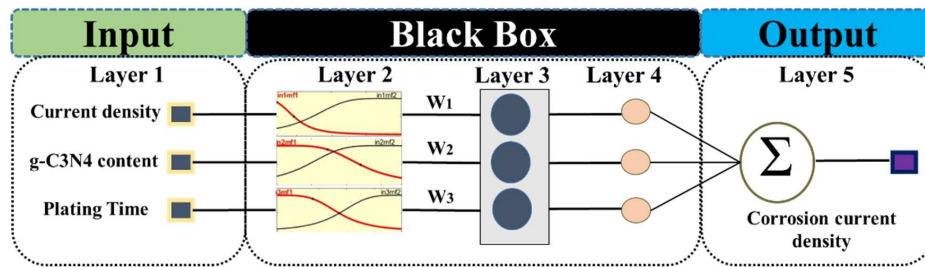


Fig. 3. Typical structure of the ANFIS model for modeling the corrosion current density of Ni/g-C₃N₄ nanocomposite coatings; the model comprises 3 inputs and 5 layers.

2.7.1 ANN modeling

ANN is known as a computational approach that includes various biological neural structures. In this computational method, the appropriate relationships among input and output variables can be achieved without any prerequisite. The three-layer fundamental structure of a neural network comprises an input, hidden, and output layers [33]. Accordant with the dataset, current density, g-C₃N₄ content, and plating time were set as the inputs for each model. The structure of ANN modeling employed in this study was shown in Fig. 2. Each layer contains the basic factor neurons, which are processing factors. The neuron calculates the weight of each input with a special weight index (*w*) which is received from the signal of an output. The total weights of the inputs show the bias (*b*) and the transfer function $f(\sum w_i x_i)$. Thus, the neurons in different layers are connected together. Finally, nonlinear mapping has been connected the input layer to the output layer. A transfer function or activation function turns the signal data that moves between each neuron. One of the crucial parts in the accuracy of the constructed model is the arrangement of hidden layers. In the hidden layer, the learning process take place and also the quantity of each independent parameters were received [34].

The performance and convergence of the ANN model are highly affected by the number of hidden layers and neurons in each hidden layer. Even though, for a small dataset, usually, a single hidden layer resulted in more accuracy and convergence in comparison with two hidden layers. However, these two elements have an important effect on the efficiency of an ANN model. It was preferred to search for the best ANN architecture, such as a model with an optimizing training algorithm and the number of neurons in each hidden layer [35]. Thus, we seek to produce an appropriate structure with one hidden layer for the ANN model. To find a suitable number of neurons, various topological research has been done. The results represent that number of hidden layers is changeable, and the best structure has the least error. For training, the Levenberg–Marquardt back propagation (LMBP) algorithm was employed. LMBP has been widely used in prior research and is well-known for its speed, processing power, reliability, and simplicity [22]. Therefore, for changing the number of neurons LMBP training algorithm was utilized. Hyperbolic tangent sigmoid and Purlin were used as transfer functions for hidden layer and output layer in the ANN modeling. Several studies showed that fewer neurons had resulted in under fitting, and more neurons could result in over fitting, so that trial and error is required to extend the trustable structure for ANN [36]. In this study, ANN was computed with the ANN toolbox in MATLAB software.

2.7.2 ANFIS modeling

Constructing the network structure or Takagi-Sugeno fuzzy inference system has been done by "if-then" rules of the ANFIS model [37]. As presented in Fig. 3, the structure of the ANFIS model comprises of five layers. The input membership functions (MFs) in the first layer transport the inputs to a fuzzy set. Then, in the second layer fixed nodes are used to measure the firing strength. The firing strength is a quantity to which a fuzzy rule's antecedent part is fulfilled and determined by an AND or OR operation, and it shapes the output function for the rule. After that, in the third layer, firing strength values are done by the normalization process. To determine the impact of the output to the total output in the next layer, the parameter set is multiplied by the output of the prior layer. The summation of each input's signal is determined in the fifth layer.

Grid partition (GP) is known as one of the methods for producing the ANFIS structure from available data. It has been reported that as the number of inputs increase, the number of fuzzy rules grows exponentially. Also, a GP technique is only appropriate for a dataset which consist of less than six inputs parameters [39, 40]. In this study, we selected ANFIS-GP, in which different types of MF for each input parameter and linear type of MF for output were used to optimize the fuzzy model.



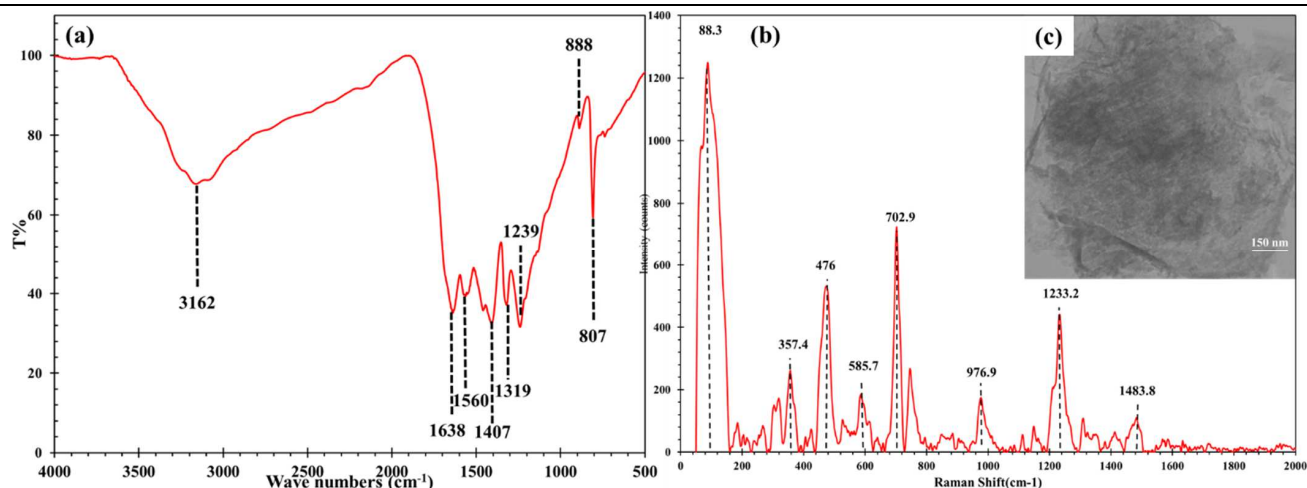


Fig. 4. (a) FTIR, (b) Raman spectra and (c) TEM image of g-C₃N₄ nanosheets.

3. Results and Discussion

3.1 Characterization of g-C₃N₄ nanosheets

The g-C₃N₄ nanosheets were characterized by FTIR (Fig. 4a). A broad peak located at 3162 cm⁻¹ was associated with the stretching vibration of N-H bonds [41]. Also, a series of peaks at 1638, 1560, 1407, 1319, and 1239 cm⁻¹ can be referred to as the stretching vibration of C-N or C=N in the CN heterocycles of g-C₃N₄ heptazine structures [42]. It was clear that the absorption at 810 cm⁻¹ is indicative of out-of-plane bending modes of the rings [43]. Raman spectrum of the g-C₃N₄ nanosheets is provided in Fig. 4b. It was revealed that there are two peaks observed at 1233 cm⁻¹ and 1483 cm⁻¹. These peaks may relate to some disorder or defects in the g-C₃N₄ structure [59, 60]. What is more, the strong peaks raised at 702 cm⁻¹ may represent the g-C₃N₄ structure or be attributed to the bending vibrations of melamine, according to [61]. Moreover, the Raman spectrum showed several strong, distinctive peaks of g-C₃N₄ detected at 88.3, 476 and related to heptazine rings in melamine units [44, 62]. TEM image of g-C₃N₄ reported in Fig. 4c reveals an irregular shape for g-C₃N₄ in nanoscale.

3.2 Effect of current density

Fig. 5 illustrates the morphologies of Ni/g-C₃N₄ coatings which are applied at various current densities. The presence of pinholes and pits on the Ni coatings surfaces might be related to the reduction of hydrogen ions and/or the impurities in the solution reported previously [52]. At lower current density (e. g. 0.02 and 0.05 A.cm⁻²), the electrodeposited surface is smooth, but some defects such as nodules and pinholes were observed on the surface, as depicted in Fig. 5a-d. At a medium current density of 0.1 A.cm⁻², a uniform deposition was obtained, leading to 'defects' reduction in the coatings (Fig. 5e & f). At 0.2 A.cm⁻², some cracks were observed, as shown in Fig. 5g-l. Thus, the current density of 0.1 A.cm⁻² was chosen as the optimum current density for the electrodeposition of Ni/g-C₃N₄ nanocomposite coatings, according to better surface morphology.

Fig. 5i-k shows the EDS mapping of Ni/g-C₃N₄ nanocomposite coating, indicated that nanocomposite consists of Ni, C, and N elements, and it was proved that g-C₃N₄ nanosheets and Ni were uniformly distributed throughout the coating. Moreover, the EDX measurements (Table 2) showed that the amount of Ni in the deposit grew as the current density raised. This behavior could relate to the increasing of Coulomb force between Ni²⁺ adsorbed on g-C₃N₄ particles and the cathode with increasing current density. However, by increasing the current density the content of g-C₃N₄ in the coating dropped which may attributed due to the rapid deposition of the metal matrix and fewer particles are embedded into the coating [63].

The polarization plots of the Ni/g-C₃N₄ coatings with various current densities and 0.5 g/L of g-C₃N₄ are plotted in Fig. 6. Table 3 presents the electrochemical parameters extracted from the polarization plots, containing polarization resistance (*R_p*), cathodic Tafel slopes (*b_a* and *b_c*), corrosion potential (*E_{corr}*), and corrosion current density (*i_{corr}*). The Ni/g-C₃N₄ with 0.02 A.cm⁻² current density had the most negative *E_{corr}* and the highest *i_{corr}* demonstrating its worst corrosion resistance. However, at 0.1 A.cm⁻² current density, Ni/g-C₃N₄ nanocomposite coating presented the most positive *E_{corr}* and the lowest *i_{corr}* which clearly showed that it had the highest corrosion resistance. This result can be originated from the higher integrity of the deposited film as depicted in SEM-EDS results.

Table 2. Percentage of element EDS analysis of Ni/g-C₃N₄ nanocomposite coatings at various current densities and 0.5 g/L of g-C₃N₄.

	Ni/g-C ₃ N ₄ @ 0.02 A.cm ⁻²	Ni/g-C ₃ N ₄ @ 0.05 A.cm ⁻²	Ni/g-C ₃ N ₄ @ 0.1 A.cm ⁻²	Ni/g-C ₃ N ₄ @ 0.2 A.cm ⁻²
Ni (%w)	92.81	93.09	94.24	91.35
C (%w)	4.29	4.46	3.99	6.32
N (%w)	2.90	2.46	1.77	2.33

Table 3. Electrochemical parameters of the Ni/g-C₃N₄ coatings with different current densities derived from polarization curves are shown in Figure 6.

Current density (A.cm ⁻²)	<i>E_{corr}</i> (mV vs SCE)	<i>i_{corr}</i> (μA.cm ⁻²)	<i>b_a</i> (mV.decade ⁻¹)	<i>b_c</i> (mV.decade ⁻¹)	<i>R_p</i> (Ω.cm ²)
0.02	-374.0± 35	8.4± 0.8	26 ± 10	127± 30	1118± 328
0.05	-203.7± 7	5.4± 0.5	53± 10	122± 20	2976± 209
0.1	-125.5± 8	2.5± 0.2	35± 10	94± 10	4535± 187
0.2	-244.4± 11	3.6± 0.4	49± 10	61± 10	3277± 268



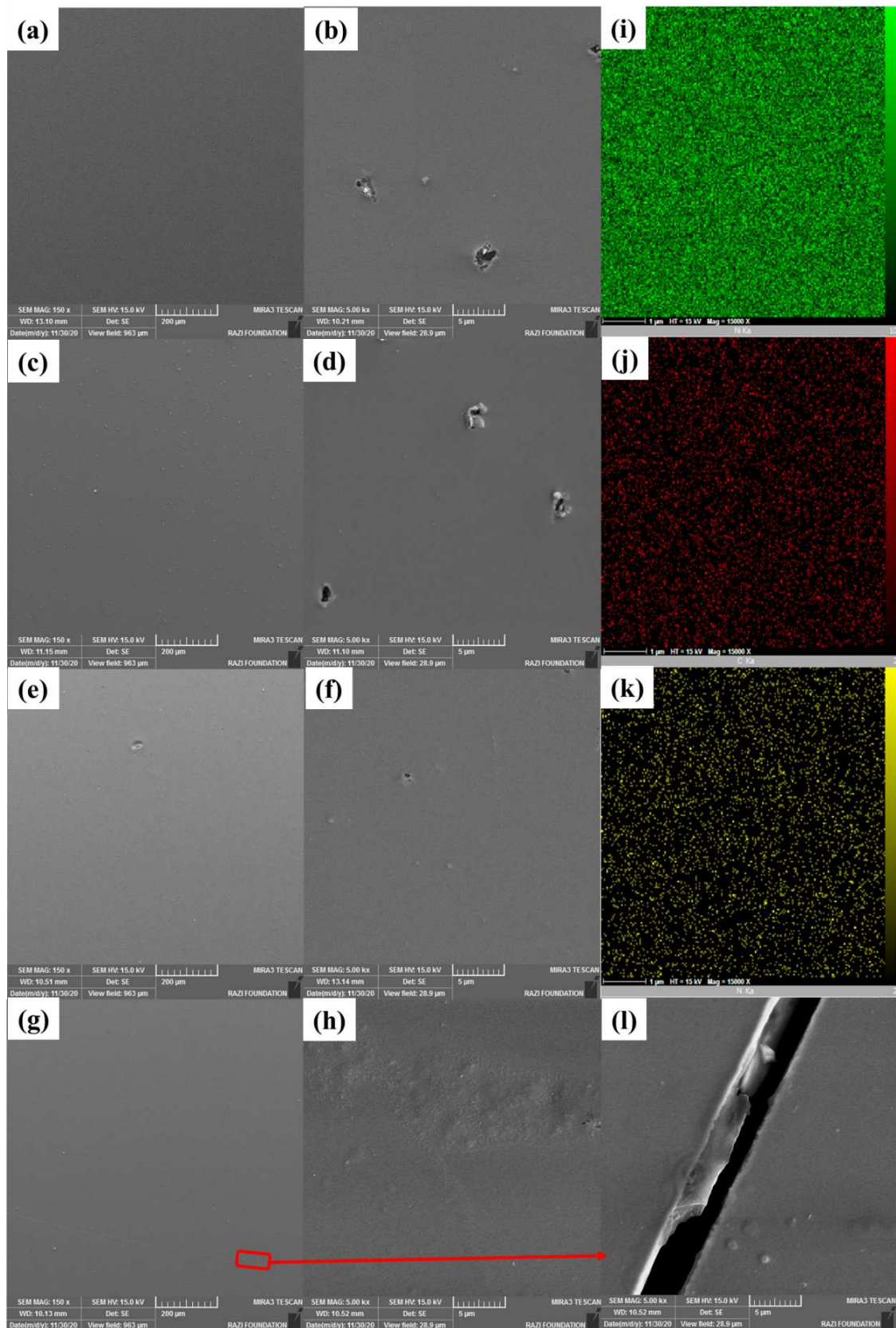


Fig. 5. SEM micrographs for the Ni/g-C₃N₄ nanocomposite coatings at various current densities and 0.5 g/L of g-C₃N₄: 0.02 (a, b), 0.05 (c, d), 0.1 (e, f) and 0.2 A.cm⁻² (g, h, l); EDS dot-mapping images of 0.1 A.cm⁻² sample.

EIS was applied to assess the impact of current density on the corrosion resistance of Ni/g-C₃N₄ coatings. Fig. 7 illustrates Nyquist and typical Bode diagrams of Ni/g-C₃N₄ coatings at different current densities. The results revealed that at 0.1 A.cm⁻² current density, the highest impedance was achieved, which is in agreement with the polarization results.



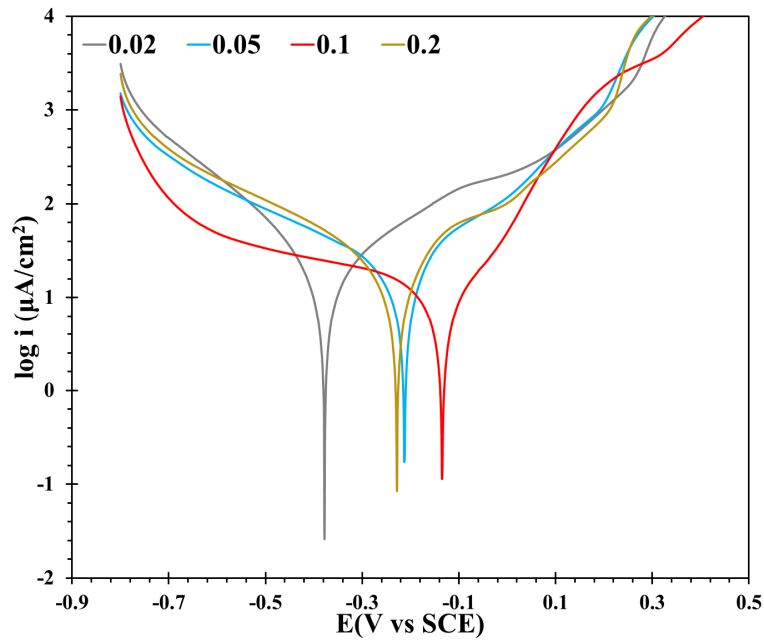


Fig. 6. Polarization curves for the Ni/g-C₃N₄ coatings with different current densities and 0.5 g/L of g-C₃N₄ in a 3.5 wt% NaCl solution at room temperature.

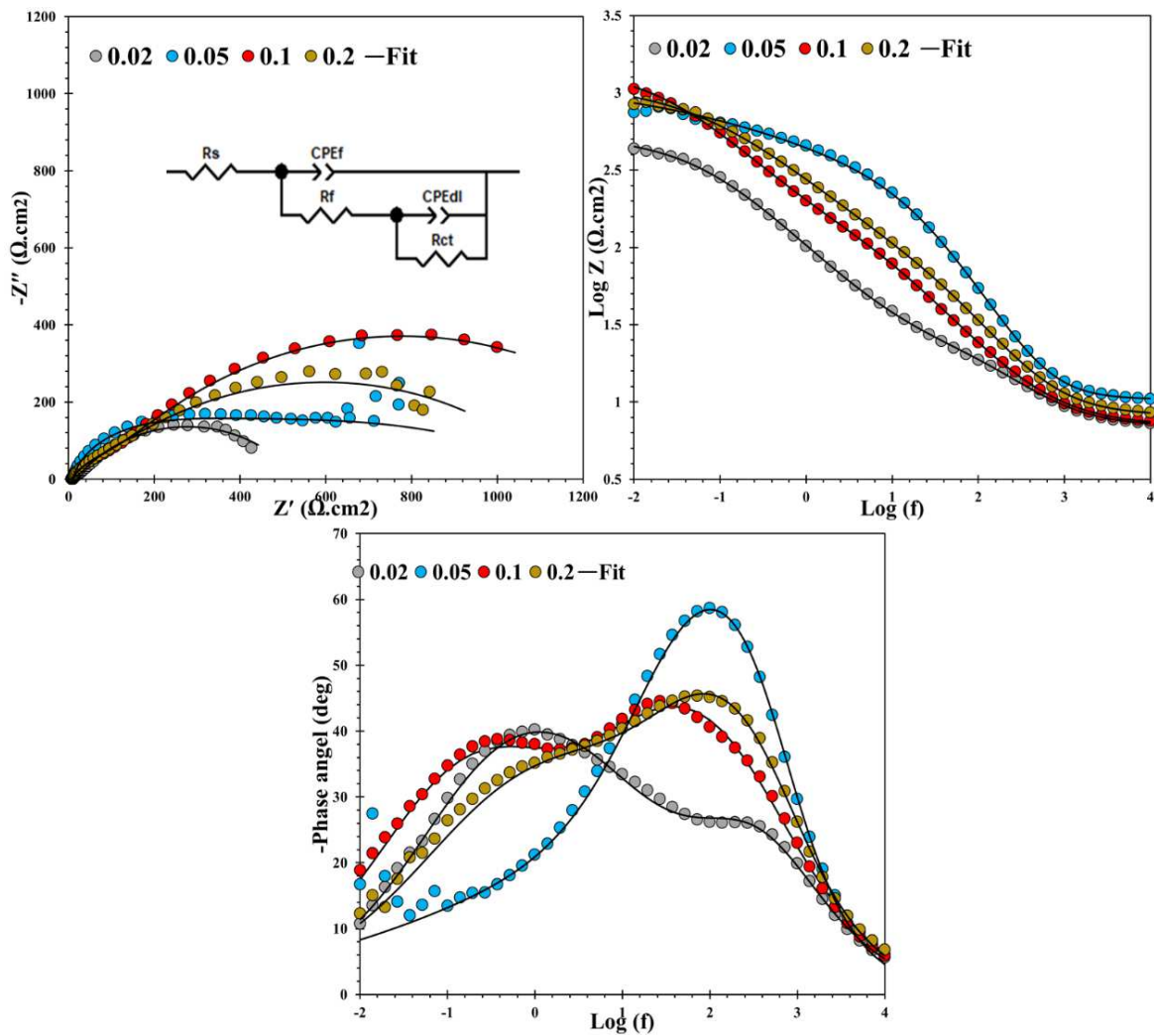


Fig. 7. The Nyquist, corresponding Bode and phase angle plots of the electrolysis Ni/g-C₃N₄ coatings with different current density and 0.5 g L⁻¹ of g-C₃N₄ in a 3.5 wt% NaCl solution at room temperature.



Table 4. Electrochemical parameters obtained by fitting the measured EIS data (Figure 7) for the deposited Ni/g-C₃N₄ coatings with current density in a 3.5 wt% NaCl solution at room temperature.

Current density (A.cm ⁻²)	R _s (Ω.cm ²)	CPE _f		R _f (Ω.cm ²)	CPE _{dl}		R _{ct} (Ω.cm ²)	Z-module (Ω.cm ²)
		Y ₀ (μΩ ⁻¹ .cm ⁻² s ⁿ)	n		Y ₀ (μΩ ⁻¹ .cm ⁻² s ⁿ)	n		
0.02	6.9± 0.2	376± 38.2	0.73± 0.02	19.2± 9.6	2913± 153	0.61± 0.02	509.1± 75.5	535.2± 66.5
0.05	10.3± 0.3	51.6± 11.4	0.91± 0.01	103± 16.3	1092± 128	0.32± 0.01	1090± 59.7	1203.3± 98.2
0.1	6.9± 0.2	629± 62.7	0.67± 0.02	175.2± 22.5	1747± 112	0.61± 0.02	1291± 42.7	1473.1± 58.7
0.2	8.1± 0.2	200± 35.9	0.77± 0.02	94.4± 18.3	1289± 134	0.52± 0.02	1059± 77.2	1161.6± 88.3

Table 5. Electrochemical parameters of the Ni and Ni/g-C₃N₄ coatings with different g-C₃N₄ concentration and 0.1 A/cm² current density derived from polarization curves shown in Figure 8.

Conc. (g/L)	E _{corr} (mV vs SCE)	i _{corr} (μA.cm ⁻²)	b _a (mv/decade)	b _c (mv/decade)	R _p (Ω cm ²)
Ni-0	-333.1± 42	7.44± 0.5	42± 10	42± 10	1126± 210
Ni-0.3	-108.4± 9	1.10± 0.1	29± 10	49± 10	4350± 195
Ni-0.9	-133.2± 12	1.96± 0.1	37± 20	48± 10	4636± 322
Ni-1.8	-197.4± 11	2.76± 0.1	33± 10	45± 10	2976± 336

To interpret the impedance diagrams in more detail, the equivalent circuit depicted in Fig. 88 has been used. In this circuit, R_s indicates the solution resistance, R_{ct} for the charge transfer resistance, R_f for the film resistance. CPE_{dl} and CPE_f are related to the double layer and film constant phase elements, respectively. Constant phase element (CPE) was utilized as a substitute of C because of the capacitor's non-ideal behavior. The exponent (0<n<1) and admittance of CPE, are represented by Y₀ and n in CPE, respectively. Table 4 gives the values of electrochemical parameters obtained from impedance spectra. The increase in current density from 0.02 to 0.1 led to an increase in R_f. The highest R_f was observed at 0.1 A.cm⁻², which is in agreement with polarization test results. The higher coating integrity determined at 0.1 A.cm⁻² might be the reason for its superior corrosion resistance. Moreover, in the case of R_{ct} values, one can deduce that the sample with 0.1 A.cm⁻² provided the highest degree of protection in comparison with the rest of the samples.

3.3 Effect of g-C₃N₄ content and plating Time

In this section, the influence of various g-C₃N₄ content (0.3, 0.9, and 1.8 g/L) in the electrolysis bath of Ni/g-C₃N₄ coating prepared at 0.1 A.cm⁻² was studied. Fig. 8 presents the polarization plots of Ni and Ni/g-C₃N₄ coatings with various g-C₃N₄ content. The electrochemical variables derived from the coatings' polarization plots are reported in Table 5. Obviously, the presence of g-C₃N₄ shifted the E_{corr} to more positive values, resulting in a change of the i_{corr} to 1.10 μA.cm⁻² for 0.3 g/L g-C₃N₄. It has been understood that, in comparison to composite coatings with lower g-C₃N₄ concentrations, an increase in the i_{corr} value and more negative value of E_{corr} was achieved by increasing the g-C₃N₄ content.

Fig. 9 displays the Nyquist, phase angle, and Bode diagrams of the electrolysis Ni/g-C₃N₄ coatings with different g-C₃N₄ concentrations at 0.1 A/cm² current density. Changing the amount of g-C₃N₄ in the electrolysis bath affected the EIS results. As depicted in Fig. 9, when 0.3 g/L g-C₃N₄ was used in the Ni/g-C₃N₄ coating, the spectra showed only one relaxation time, while for the rest of the samples, two relaxation times were observed. Detection of only one-relaxation time in the case of 0.3 g/L g-C₃N₄ might be originated from its highest integrity leading to the occurrence of corrosion only at the Ni surface. The rest of the samples have defects in the Ni deposited film, which lead to the occurrence of corrosion at the defect areas as Ni is more noble than Fe. Table 6 displays the values of electrochemical parameters derived from impedance spectra.

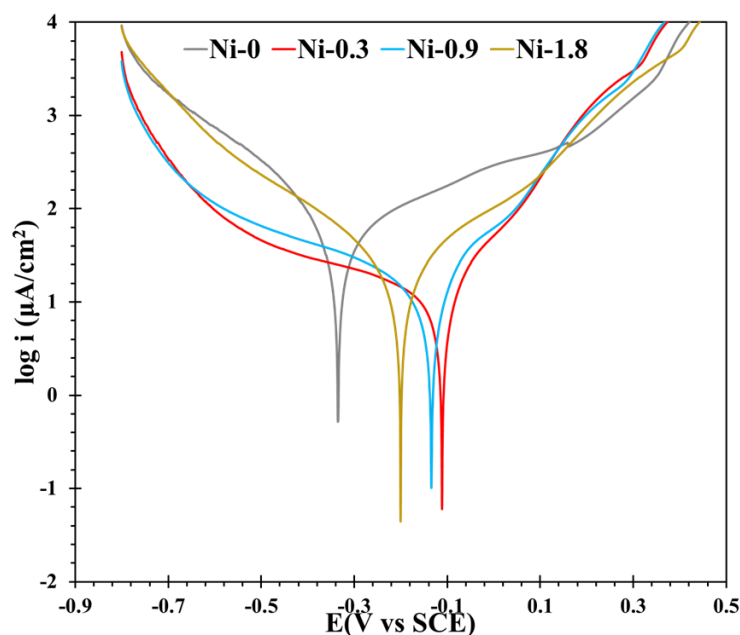


Fig. 8. Tafel polarization curves for the Ni and Ni/g-C₃N₄ coatings with different g-C₃N₄ concentration and 0.1 A/cm² current density in a 3.5 wt% NaCl solution at room temperature.



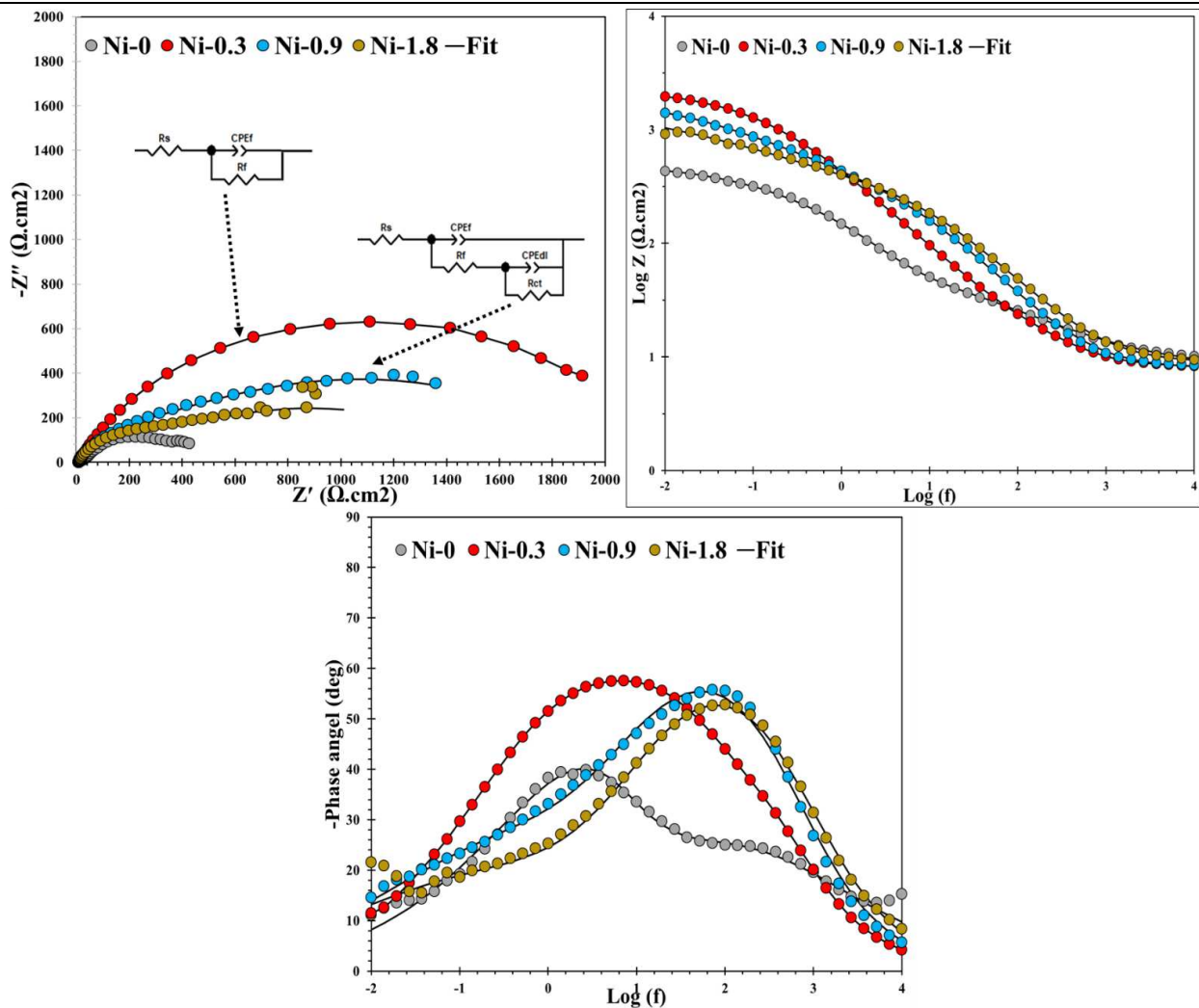


Fig. 9. The Nyquist, corresponding Bode and phase angle plots of the Ni/g-C₃N₄ coatings with different g-C₃N₄ concentration and 0.1 A/cm² current density in a 3.5 wt% NaCl solution at room temperature

The highest charge transfer resistance was obtained in the presence of 0.3 g/L g-C₃N₄, which implies the best protection of this electrodeposited coating. By increase in extend of g-C₃N₄, R_{ct} showed a decrease which can be originated from the formation of more defects in the coating.

Moreover, the influence of plating time was investigated utilizing a polarization test. The values of current density and g-C₃N₄ concentration were set at 0.1 A.cm⁻² and 0.3 g/L. The polarization curves and corresponding electrochemical parameters for Ni/g-C₃N₄ coating at various plating times were illustrated in **Supporting Information** (Fig. S1 & Table S1). The results revealed that at 45 min, higher corrosion resistance was obtained as compared to other plating time values.

The XRD pattern for pure Ni coating and Ni/g-C₃N₄ coating with 0.3 g/L of g-C₃N₄ and 0.1 A/cm² were shown in Fig. 10. As demonstrated all characteristic peaks of nickel crystallographic planes (111), (200), (220) are recognized. In the XRD pattern of Ni/g-C₃N₄ coating a relatively weak diffraction peak (002) can be observed at 27.8°, is corresponding to the graphite-like stacking of conjugated aromatic segments [26]. By apply the Scherrer's equation, the grain sizes in the coating structure are calculated [1]. The crystallite size for (111), (200) and (220) characteristic peaks were calculated and are reported in Table 7. It can be observed that in the Ni/g-C₃N₄ coating the intensity of the Ni (111) diffraction peak is reduced, the relative intensity of (200) and (220) crystallographic planes increases which can be indicative of preferential growth on the latter crystalline planes. Peak broadening happens in all three planes, which is believed to be an indication of grain refinement during the coatings growth. During the incorporation of reinforcing g-C₃N₄ nanosheets in the coating structure, the number of nucleation sites for nickel increases and the crystal growth is retarded [13, 16].

Table 6. Electrochemical parameters obtained by fitting the measured EIS data (Figure 9) for the deposited Ni/g-C₃N₄ coatings with different g-C₃N₄ concentration in a 3.5 wt% NaCl solution at room temperature.

Con. (g/L)	R _s (Ω.cm ²)	CPE _f		R _f (Ω.cm ²)	CPE _{dl}		R _{ct} (Ω.cm ²)	Z-module (Ω.cm ²)
		Y0 (μΩ ⁻¹ .cm ⁻² s ⁿ)	n		Y0 (μΩ ⁻¹ .cm ⁻² s ⁿ)	n		
Ni-0	7.8± 0.3	1793± 195	0.49± 0.01	78.74± 28.6	355.1± 86.1	0.93± 0.02	428± 95.5	514.5± 52.7
Ni-0.3	7.9± 0.1	-	-	-	595± 49.5	0.69± 0.01	2117± 33.8	2124.8± 92.1
Ni-0.9	7.9± 0.3	184± 25.6	0.78± 0.01	300± 22.4	1312± 132.6	0.47± 0.01	1734± 81.7	2041.9± 112.8
Ni-1.8	8.8± 0.2	152± 48.2	0.77± 0.02	286.8± 11.5	2018.1± 216.9	0.43± 0.01	1300± 102.2	1595.6± 142.5

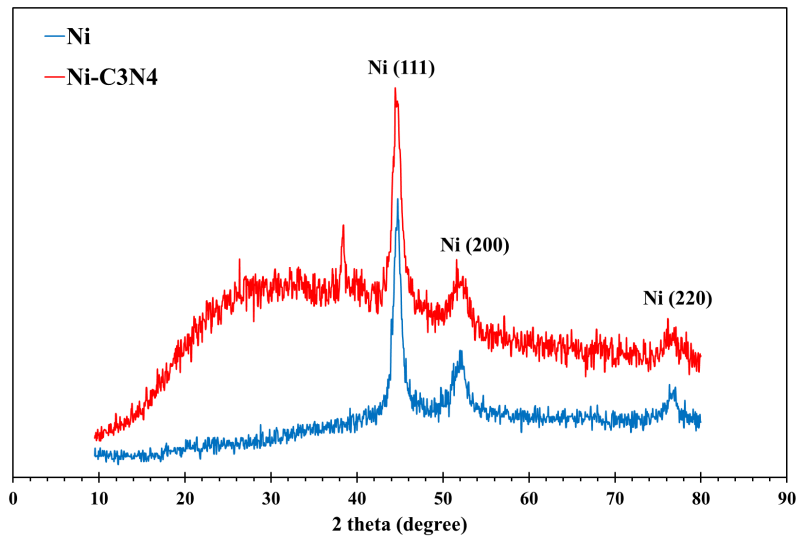
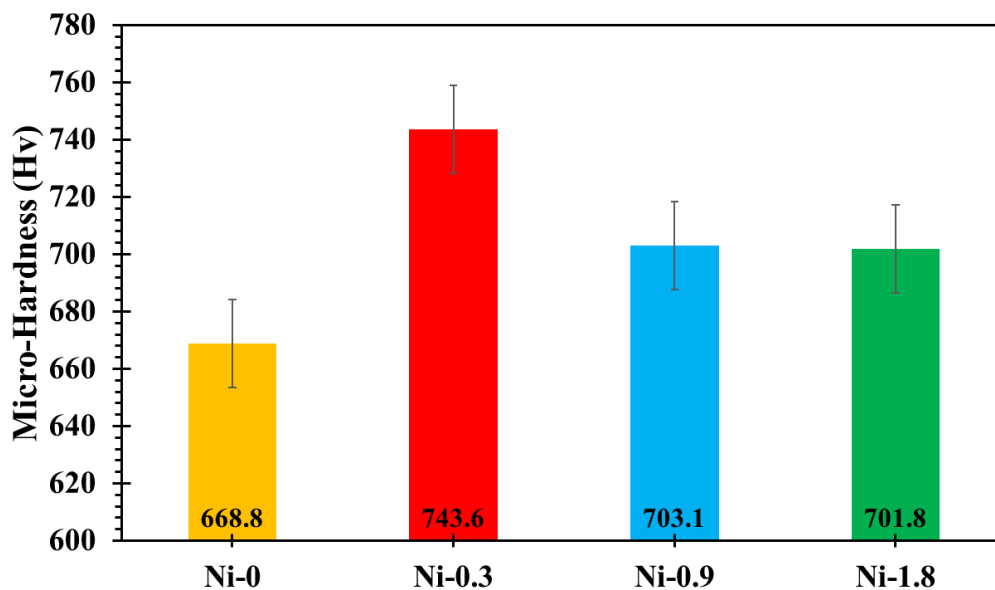


Table 7. XRD analysis results for pure Ni and Ni/g-C₃N₄ coating samples.

Sample	Plane	Peak position, 2θ (degrees)	Peak broadening	Crystallite size (nm)
Pure Ni Coating	(111)	45.1	0.51	16.9
	(200)	52.5	0.70	12.7
	(220)	76.9	0.76	13.3
Ni/g-C ₃ N ₄ coating	(111)	45.2	0.63	13.9
	(200)	52.6	0.89	10.3
	(220)	77.2	1.04	9.8

3.4 Microhardness

The microhardness of the Ni/g-C₃N₄ coatings at different concentrations of g-C₃N₄ nanosheets in the deposited coatings is presented in Fig. 11. As can be seen clearly, the microhardness increased with the presence of g-C₃N₄ in the bath. Although all the Ni/g-C₃N₄ nanocomposite coatings showed better results compared to the purely Ni coating, the higher loading levels depicted a negative effect on the microhardness. The microhardness of the electrodeposited nickel with 0.3 g/L of g-C₃N₄ showed a maximum value of 743.6 HV that could be related to the stronger bonding strength between the Ni matrix and the dispersed g-C₃N₄. Beyond 3 g/L of g-C₃N₄, the microhardness was approximately constant. It has been reported that the hardness behavior of Ni composite coatings is influenced by several factors such as; grain size, the distribution and amount of reinforcement (e. g. g-C₃N₄), chemical composition of the Ni, and microstructure variation caused by the nanoparticles' inclusion [47, 48]. The nano g-C₃N₄ acts as an obstacle versus dislocation movement while the Ni matrix gains the load. According to the above discussion, it can be concluded that Ni/g-C₃N₄ with 0.3 g/L of g-C₃N₄ possess the most compact structure, and the grain refinement that influenced the nucleation of small grains around the hard particles also obstruct the dislocation movement, which can lead to raising the microhardness of the nanocomposite coating (Hall-Petch relation) [53].

Fig. 10. XRD pattern for pure Ni coating and Ni/g-C₃N₄ coating with 0.3 g/L of g-C₃N₄ and 0.1 A/cm².Fig. 11. The microhardness of the Ni/g-C₃N₄ coatings for different content of g-C₃N₄ deposited at 0.1 A/cm².

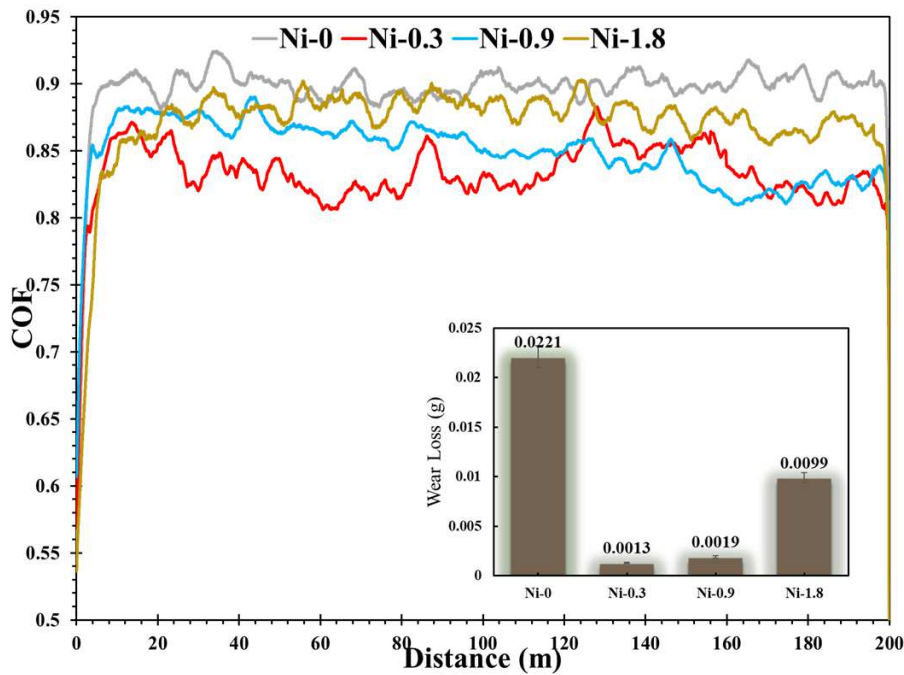


Fig. 12. The COF vs. sliding distance for Ni/g-C₃N₄ coatings at different content of g-C₃N₄ deposited at 0.1 A/cm².

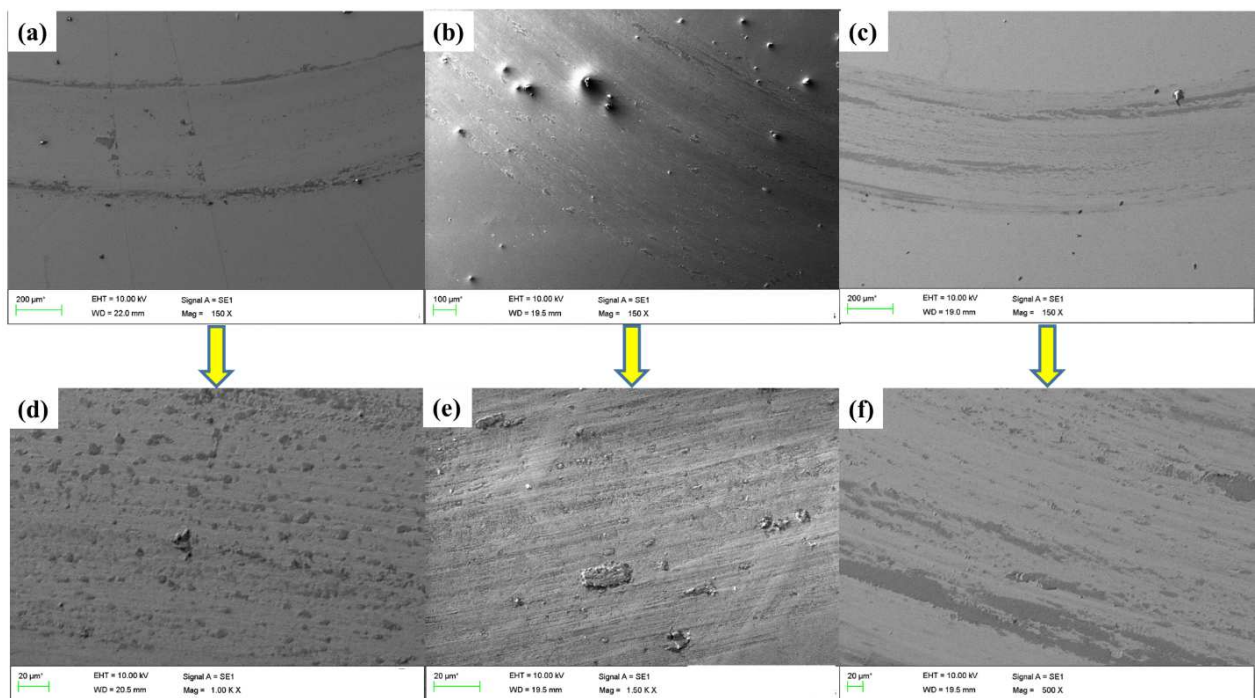


Fig. 13. SEM micrographs of the worn surface of Ni/g-C₃N₄ coatings at different content of g-C₃N₄ (a) pure Ni, (b) Ni-0.3 g/L and (c) Ni-0.9 g/L deposited at 0.1 A/cm² after wear test and their corresponding high magnification images (d, e and f, respectively).

3.5 Wear resistance

In Fig. 12, the coefficient of friction (COF) vs. sliding distance of all electrodeposited Ni/g-C₃N₄ coatings at different content of g-C₃N₄ is demonstrated. As shown, COF started with a low value, and after that, there was sudden incensement due to the generation of wear particles. However, a stable friction behavior was observed from 20 to 120 m. At a greater distance, there was a reduction in COF owing to softening the coating surface. The COF curve of the coatings steadily augmented to a specific value, and it remained at this certain value of friction coefficient after sliding for 200 m. It is observed that all Ni/g-C₃N₄ coatings had less friction coefficient than pure nickel coatings and the sample with 0.3 g/L g-C₃N₄ showed the COF of 0.83, which was the lowest value compared to other coated samples. The average coefficient of friction of other samples with 0.9 and 1.8 g/L g-C₃N₄ was 0.84, 0.89, respectively.

While the surface of Ni/g-C₃N₄ was eliminated during the sliding process, the existence of g-C₃N₄ caused a reduction in shear stress which reduced the COF value. Due to the reduction of COF, the Ni/g-C₃N₄ coatings displayed lower surface roughness and fewer cracks [54]. It can be observed from Fig. 12 that the highest COF value belonged to the pure Ni coating with 0.89 average COF, which could lead to increased surface roughness and influence the wear losses and cause larger wear grooves. Moreover, the weight loss data for Ni nanocomposite coatings after the wear test were reported in Fig. 12. The lowest weight loss for 0.3 g/L g-



C₃N₄ represents the higher wear behavior of this sample. Fig. 13 shows the SEM worn morphologies of Ni/g-C₃N₄ coatings and pure Ni after the wear test. The wear surface morphologies of the pure Ni coating revealed huge grooves on the worn surfaces, whereas the Ni/g-C₃N₄ coating with 0.3 g/L g-C₃N₄ showed only a few small pits, explaining and approving the coating's highest wear resistance.

Moreover, the cross-sectional SEM morphologies of Ni/g-C₃N₄ nanocomposite coating prepared at 0.3 g/L g-C₃N₄, 0.1 A/cm² current density and 45 min plating time was shown in Fig. 14. It can be seen that the average thickness of the coating is about 39.97 μ m. It is apparent that the coatings show a compact structure and a suitable adhesion between the coating and substrate has been observed.

3.6 Modeling Results

As mentioned in modeling details, the purpose is to provide an optimized model for corrosion behavior of Ni/g-C₃N₄ coatings. As demonstrated in Fig. 15, the change of neurons in the hidden layer from 2 to 10 resulted in variation of ANN model performance. Variation of R² was observed by changing the neurons in the hidden layer from 2 to 10. Four neurons' hidden layer architecture was used as it led to the highest R² values resulting in the most trustable results

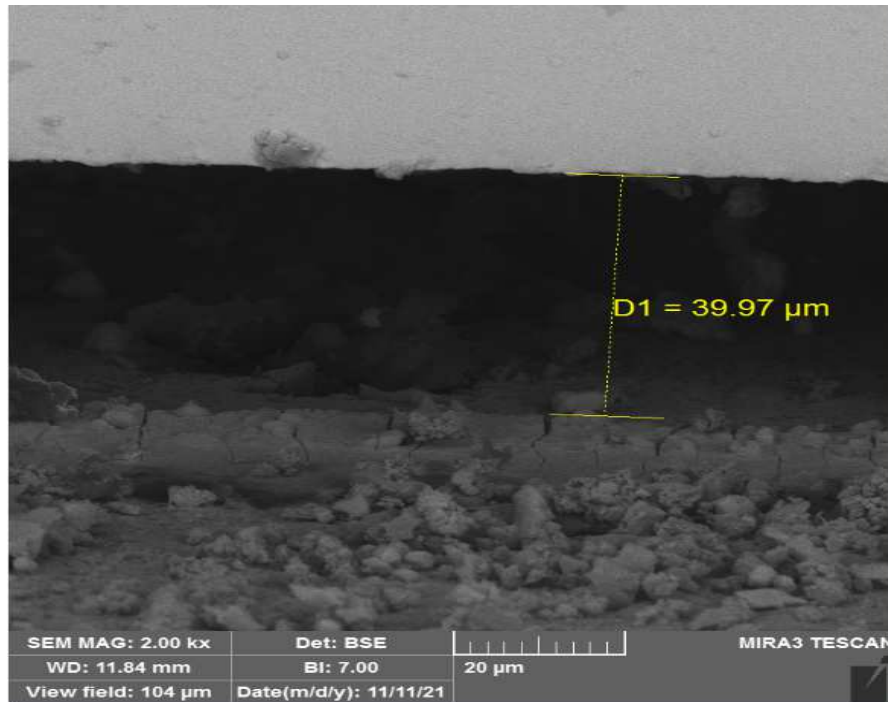


Fig. 14. Cross-sectional SEM morphologies of Ni/g-C₃N₄ nanocomposite coating prepared at 0.3 g/L g-C₃N₄, 0.1 A/cm² current density and 45 min plating time.

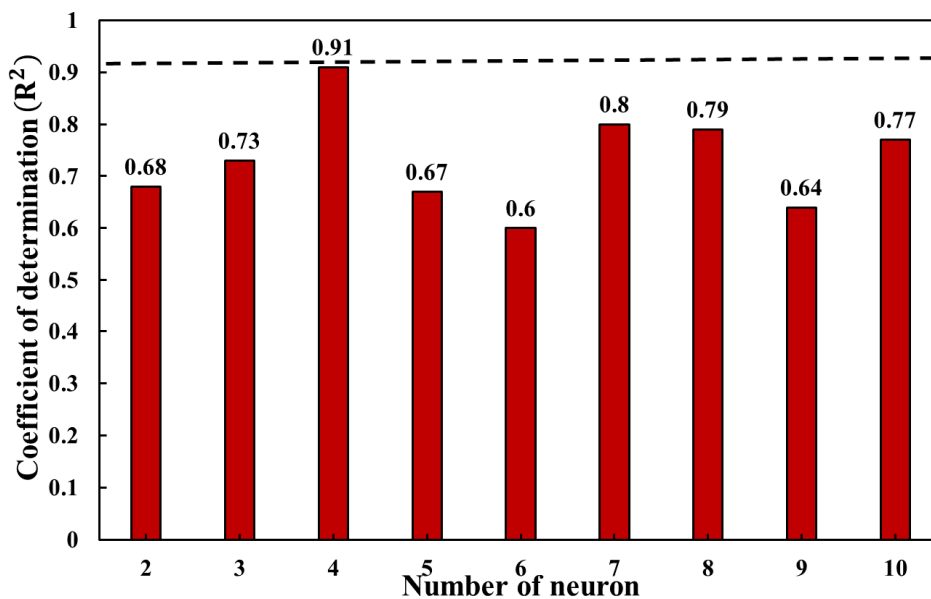


Fig. 15. The variation of R² for ANN model with different number of neurons from 2 to 10 in the hidden layer.



Table 8. The effect of training algorithm on the performance of the seven ANN models executed with four neurons in the hidden layer architecture.

ANN models	Training Algorithm	Symbol	MAE	MSE	R ²
ANN-1	Resilient backpropagation	RP	1.139	2.051	0.58
ANN-2	BFGS quasi-Newton backpropagation	BFG	0.7881	1.932	0.71
ANN-3	Scaled Conjugate Gradient	SCG	1.058	3.158	0.52
ANN-4	Levenberg–Marquardt backpropagation	LM	0.554	0.580	0.91
ANN-4	Gradient Descent with Momentum & Adaptive LR	GDX	1.367	3.156	0.53
ANN-6	Conjugate Gradient With Powell/Beale Restarts	CGB	0.911	1.707	0.74

Table 9. The performance of alternative ANFIS-GP models.

ANFIS-models	Membership function name	Symbol	MSE	MAE	R ²
ANFIS-GP1	Triangular-shaped	Trimf	0.0045392	0.042794	0.999319
ANFIS-GP2	Trapezoidal-shaped	Trapmf	0.1972406	0.217367	0.970417
ANFIS-GP3	Generalized bell-shaped	Gbellmf	0.0001676	0.007020	0.999974
ANFIS-GP4	Gaussian curve	Gaussmf	0.0067303	0.04366	0.998990
ANFIS-GP5	Gaussian combination	Gauss2mf	0.0004915	0.012861	0.999926
ANFIS-GP6	Difference between two sigmoidal	Dsigmf	0.0004924	0.012872	0.999926

Accordingly, for further optimization of the training phase, a single hidden layer that consists of four neurons and the mentioned transfer functions were used. For this, seven various ANN structures were administrated to get the suitable training algorithm for the prediction of the corrosion current densities of Ni/g-C₃N₄ coatings. In order to construct the optimal ANN model, the MSE, MAE, and R² values of the built models were compared (Table 8).

The ANN-4 model has been chosen since it has the lowest MAE, MSE (0.554, 0.580), and a higher coefficient of determination than that of the other models (0.91). For the case of the ANFIS model, to obtain the optimum type of MF with the least error, six types of MFs were adjusted. It was observed that Gbellmf had the lowest error value. Therefore, it was selected as the optimum MF of this model. Table 9 depicts the variation for all models.

The reliability of constructed models was examined to value the precision of each model. As discussed above, the best ANN structure was chosen, with four neurons in a single hidden layer. The LM presented a better performance for the purpose of the training model; hence, the offered ANN model for anticipating the dataset obtained the lowest MAE and MSE values. Moreover, to construct the best ANFIS structure for predict the corrosion current density of Ni/g-C₃N₄ nanocomposite coatings, several models were built. ANFIS-GP3 with MSE and MAE values of 0.0001676 and 0.007020 showed the highest performance.

Fig. 16 shows the relation between experimental (observed) and modeling (predicted) amounts of corrosion current density achieved by ANN and ANFIS models. Generally, the accumulation of data points around the Y=X line displays that the anticipation of the experimental data is achieved with higher accuracy. The points near the regression line proved the efficiency of the developed model. In addition, the amount of R² for ANFIS and ANN models were 0.99 and 0.91, respectively, and proved that both models could appropriately predict the corrosion current density of Ni/g-C₃N₄ nanocomposite coatings. Based on the reported errors (R², MSE, MAE), even though ANN displayed a reliable performance, it is explicit that the predictive potential of ANFIS model is higher compared with the ANN model.

To validate the constructed machine learning models, several parameters were utilized to evaluate the ability of each model. Smith et al. [55] reported the R formula to evaluate the performance of a constructed model. The equations are provided in Table 10. In this equation, h_i and t_i represents the observed and predicted outputs, respectively, \bar{h}_i and \bar{t}_i are the average value for corresponding parameters. Moreover, other statistical criteria were presented to the models to compare the performance. Where k is the slope of the regression line is obtained output (h_i) against anticipated output (t_i) and k' is the anticipated output versus obtained output (t_i Vs. h_i) [56]. As presented in this table, other useful parameters, such as m , n , and R_m were calculated for the models [57, 58]. The results demonstrated both machine learning models, could satisfy the mentioned standard condition for each criterion. However, the performance of the ANFIS model performed significantly better compared to the ANN model. Therefore, the ANFIS is the most accurate model to predict the corrosion behavior of Ni/g-C₃N₄ coatings.

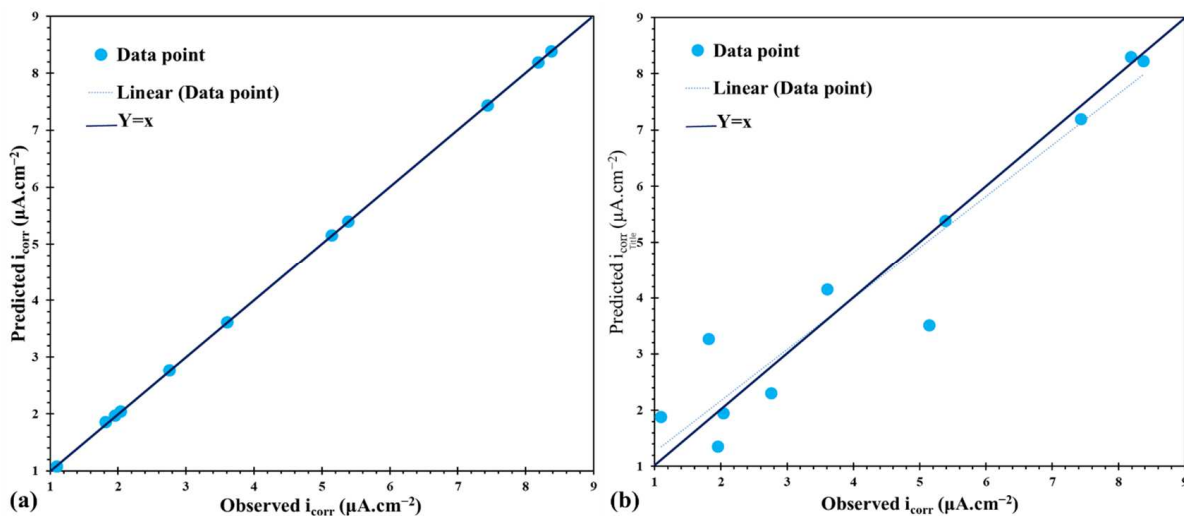


Fig. 16. The correlation of the observed and predicted corrosion current density of Ni/g-C₃N₄ nanocomposite coatings obtained by the models: (a) ANFIS and (b) ANN. The dash line shows fitted line to the modeling result and solid lines represents the line with a slope of one.



Table 10. The validation and performance of ANFIS and ANN models

Item	Formula	Condition	ANN	ANFIS
1	$R = \frac{\sum_{i=1}^n (h_i - \bar{h}_i)(t_i - \bar{t}_i)}{\sqrt{\sum_{i=1}^n (h_i - \bar{h}_i)^2} \sqrt{\sum_{i=1}^n (t_i - \bar{t}_i)^2}}$	$0.8 < R$	0.9556	0.9999
2	$k = \frac{\sum_{i=1}^n (h_i \times t_i)}{\sqrt{\sum_{i=1}^n h_i^2}}$	$0.85 < k < 1.15$	0.9710	0.9999
3	$k' = \frac{\sum_{i=1}^n (h_i \times t_i)}{\sqrt{\sum_{i=1}^n t_i^2}}$	$0.85 < k' < 1.15$	1.0065	1.0000
4	$m = \frac{R^2 - RO^2}{R^2}$	$m < 0.1$	0.091538	0.000025
5	$n = \frac{R^2 - RO'^2}{R^2}$	$n < 0.1$	0.095102	0.000025
6	$Rm = R^2 \times (1 - \sqrt{ R^2 - RO^2 })$	$0.5 < Rm$	0.649061885	0.994962713
where				
	$RO^2 = 1 - \frac{\sum_{i=1}^n (t_i - h_i^0)^2}{\sum_{i=1}^n (t_i - \bar{t}_i)^2}, h_i^0 = k \times t_i,$	≈ 1	0.996581971	0.999999980
	$RO'^2 = 1 - \frac{\sum_{i=1}^n (h_i - t_i^0)^2}{\sum_{i=1}^n (h_i - \bar{h}_i)^2}, t_i^0 = k' \times h_i,$	≈ 1	0.999835989	0.999999983

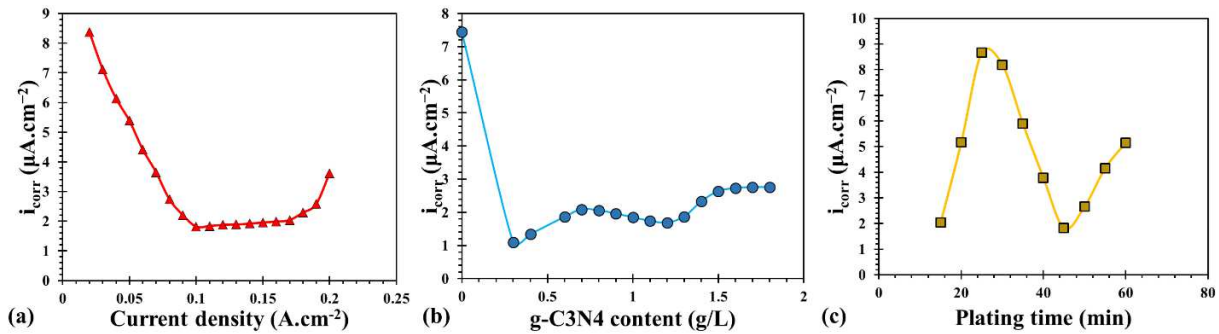


Fig. 17. The effect of electrolysis bath parameters including: (a) Current density, (b) g-C₃N₄ content, and (c) plating time on the corrosion resistance of Ni/g-C₃N₄ nanocomposite coatings. Each plot was obtained by assuming a constant value for other parameters. The assumed constant value of the current density, g-C₃N₄ content, and plating time was respectively 0.1 A.cm⁻², 0.3 g/L, and 45 min.

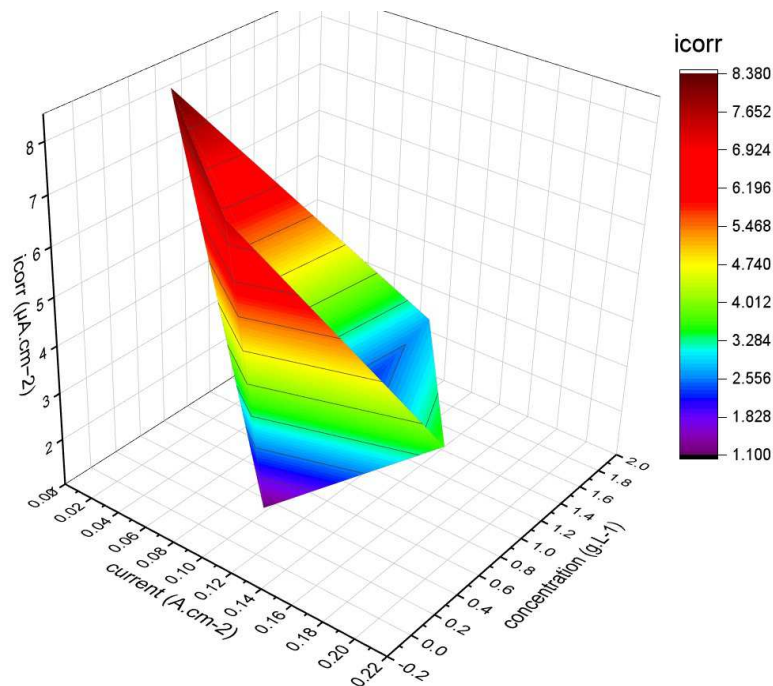


Fig. 18. Surface plot denoting the effect of current density and g-C₃N₄ content on the corrosion resistance of Ni/g-C₃N₄ nanocomposite coatings.



Finally, toward the simulation of the influence of bath parameters on the corrosion behavior of Ni/g-C₃N₄ nanocomposite coatings, the ANFIS model, which showed the highest accuracy, was used. ANFIS model has been successfully utilized to study the effect of each input parameters by the researchers [22, 26, 64]. As illustrated in Fig. 17, the corrosion current density was greatly influenced by electrolysis bath variables. In general, an increase in current density (Fig. 17a) resulted in the lower corrosion current density of Ni/g-C₃N₄ nanocomposite coatings, but the optimum value for current density was 0.1 A.cm⁻². The same behavior was observed for g-C₃N₄ content, in which 0.3 g/L resulted in a lower corrosion current density. Also, the 45 min plating time presented better corrosion resistance. These modeling results are in agreement with the outcomes of the experiments. Additionally, the 3D surface plot obtained from the ANFIS model presented in Supporting Information (Fig. S2) confirmed the mentioned results. The synergistic effects of current density and g-C₃N₄ content (concentration) on the corrosion behavior of Ni/g-C₃N₄ coatings were visualized in Fig. 18. However, the effect of current density and g-C₃N₄ content was complex. Mainly, the higher corrosion current density was achieved when the g-C₃N₄ content increases at a lower current density, which is in agreement with experimental results.

4. Conclusion

To sum up, several coatings were prepared by changing the current density and concentration of g-C₃N₄ of the electrolysis bath to study the impact of electrolysis bath parameters on the corrosion resistance of Ni/g-C₃N₄ nanocomposite coatings. The results indicated that the addition of small content of g-C₃N₄ (0.3, 0.9, and 1.8 g/L) in the electrolysis bath resulted in more compact surface morphology, better corrosion resistance, higher microhardness, and wear properties. The Ni/g-C₃N₄ coatings showed the lowest corrosion current density (1.1 μA.cm⁻²) with 0.3 g/L g-C₃N₄ and 45 min plating time. Moreover, the influence of current density on the corrosion behavior of Ni/g-C₃N₄ was investigated, which revealed the best corrosion resistance at 0.1 A.cm⁻². ANN and ANFIS machine learning models were utilized to predict the corrosion current densities of Ni/g-C₃N₄ nanocomposite coatings based on current density, g-C₃N₄ concentration, and plating time. Different ANN and ANFIS models were constructed by changing the parameters, and the most suitable ones were selected. Finally, the ANN model with the mean absolute error (MAE) value of 0.580 was achieved, which has four neurons and Levenberg–Marquardt backpropagation as a training algorithm. The mean absolute error (MAE) of the optimized fuzzy model was 7.02×10⁻³. The subsequent validity and performance analysis of the models verified that the ANFIS model was more robust than the ANN model. R² of the ANN and ANFIS models was 0.91 and 0.99, respectively. By using the ANFIS model, the corrosion current density of Ni/g-C₃N₄ coatings was predicted with higher accuracy and precision.

Author Contributions

M.R. Shishesaz and M. Mahdavian planned the scheme, initiated the project, and suggested the experiments; A. Zarezadeh, and M. Ravanavard conducted the experiments and analyzed the empirical results; M. Ghobadi and F. Zareipour developed the mathematical modeling and examined the theory validation. The manuscript was written through the contribution of all authors. All authors discussed the results, reviewed, and approved the final version of the manuscript.

Acknowledgments

Not applicable.

Conflict of Interest

The authors declared no potential conflicts of interest concerning the research, authorship, and publication of this article.

Funding

The authors received no financial support for the research, authorship, and publication of this article.

Data Availability Statements

The datasets generated and/or analyzed during the current study are available from the corresponding author on reasonable request.

References

- [1] Olia, H., Ghobadi, M., Danaee, I. and Onsoni, S., Effect of number of layers on erosion, corrosion, and wear resistance of multilayer Cr-N/Cr-Al-N coatings on AISI 630 stainless steel, *Materials and Corrosion*, 71(8), 2018, 1361-1374.
- [2] Kumaraguru, S., Kumar, G.G., Shanmugan, S., Mohan, S., Gnanamuthu, R.M., Enhanced texture and microhardness of the nickel surface using Bi₂O₃ particles via electrodeposition technique for engineering application, *Journal of Alloys and Compounds*, 753, 2018, 740-747.
- [3] Nayana, K.O., Ranganatha, S., Shubha, H.N., Pandurangappa, M., Effect of sodium lauryl sulphate on microstructure, corrosion resistance and microhardness of electrodeposition of Ni-Co₃O₄ composite coatings, *Transactions of Nonferrous Metals Society of China*, 29(11), 2019, 2371-2383.
- [4] Raghavendra, C.R., Basavarajappa, S., Sogalad, I., Saunshi, V.K., Study on surface roughness parameters of nano composite coatings prepared by electrodeposition process, *Materials Today: Proceedings*, 38, 2021, 3110-3115.
- [5] Li, B.S., Huan, Y.X., Luo, H., Zhang, W.W., Electrodeposition and properties of Ni-B/SiC nanocomposite coatings, *Surface Engineering*, 35(2), 2019, 109-119.
- [6] Li, B., Zhang, W., Huan, Y., Dong, J., Synthesis and characterization of Ni-B/Al₂O₃ nanocomposite coating by electrodeposition using trimethylamine borane as boron precursor, *Surface and Coatings Technology*, 337, 2018, 186-197.
- [7] Bagheri, P., Farzam, M., Mousavi, A.B., Hosseini, M., Ni-TiO₂ nanocomposite coating with high resistance to corrosion and wear, *Surface and Coatings Technology*, 204(23), 2010, 3804-3810.
- [8] Pingale, A.D., Belgamwar, S.U., Rathore, J.S., Effect of graphene nanoplatelets addition on the mechanical, tribological and corrosion properties of Cu-Ni/Gr nanocomposite coatings by electro-co-deposition method, *Transactions of the Indian Institute of Metals*, 73(1), 2020, 99-107.
- [9] Shelke, A.R., Balwada, J., Sharma, S., Pingale, A.D., Belgamwar, S.U., Rathore, J.S., Development and characterization of Cu-Gr composite coatings by electro-co-deposition technique, *Materials Today: Proceedings*, 28, 2020, 2090-2095.
- [10] Zhang, L., Ou, M., Yao, H., Li, Z., Qu, D., Liu, F., Wang, J., Li, Z., Enhanced supercapacitive performance of graphite-like C₃N₄ assembled with NiAl-layered double hydroxide, *Electrochimica Acta*, 186, 2015, 292-301.
- [11] Fayyad, E.M., Abdullah, A.M., Hassan, M.K., Mohamed, A.M., Wang C, Jarjoura, G., Farhat, Z., Synthesis, characterization, and application of novel




Ni-P-carbon nitride nanocomposites, *Coatings*, 8(1), 2018, 37.


- [12] Li, C., Cao, C.B., Zhu, H.S., Graphitic carbon nitride thin films deposited by electrodeposition, *Materials Letters*, 58(12-13), 2004, 1903-1906.
- [13] Fayyad, E.M., Abdullah, A.M., Mohamed, A.M., Jarjoura, G., Farhat, Z., Hassan, M.K., Effect of electroless bath composition on the mechanical, chemical, and electrochemical properties of new NiP-C₃N₄ nanocomposite coatings, *Surface and Coatings Technology*, 362, 2019, 239-251
- [14] Yang, G., Chen, T., Feng, B., Weng, J., Duan, K., Wang, J., Lu, X., Improved corrosion resistance and biocompatibility of biodegradable magnesium alloy by coating graphite carbon nitride (g-C₃N₄), *Journal of Alloys and Compounds*, 770, 2018, 823-830.
- [15] Pourhashem, S., Duan, J., Guan, F., Wang, N., Gao, Y., Hou, B., New effects of TiO₂ nanotube/g-C₃N₄ hybrids on the corrosion protection performance of epoxy coatings, *Journal of Molecular Liquids*, 317, 2020, 114214.
- [16] Yan, H., Li, J., Zhang, M., Zhao, Y., Feng, Y., Zhang, Y., Enhanced corrosion resistance and adhesion of epoxy coating by two-dimensional graphite-like g-C₃N₄ nanosheets, *Journal of Colloid and Interface Science*, 579, 2020, 152-161.
- [17] Chen, C., He, Y., Xiao, G., Zhong, F., Xia, Y., Wu, Y., Graphitic C₃N₄-assisted dispersion of graphene to improve the corrosion resistance of waterborne epoxy coating, *Progress in Organic Coatings*, 139, 2020, 105448.
- [18] Wu, L., Zhang, Z., Yang, M., Yuan, J., Li, P., Guo, F., Men, X., One-step synthesis of g-C₃N₄ nanosheets to improve tribological properties of phenolic coating, *Tribology International*, 132, 2019, 221-227.
- [19] Golafshani, E.M., Behnood, A., Arashpour, M., Predicting the compressive strength of normal and High-Performance Concretes using ANN and ANFIS hybridized with Grey Wolf Optimizer, *Construction and Building Materials*, 232, 2020, 117266.
- [20] Vakili, M., Yahyaee, M., Ramsay, J., Aghajannezhad, P., Paknezhad, B., Adaptive neuro-fuzzy inference system modeling to predict the performance of graphene nanoplatelets nanofluid-based direct absorption solar collector based on experimental study, *Renewable Energy*, 163, 2021, 807-824.
- [21] Sampath, K.H.S.M., Perera, M.S.A., Ranjith, P.G., Matthai, S.K., Tao, X., Wu, B., Application of neural networks and fuzzy systems for the intelligent prediction of CO₂-induced strength alteration of coal, *Measurement*, 135, 2019, 47-60.
- [22] Khalaj, O., Ghobadi, M., Zarezadeh, A., Saebnoori, E., Jirková, H., Chocholatý, O., Svoboda, J., Potential role of machine learning techniques for modeling the hardness of OPH steels, *Materials Today Communications*, 26, 2021, 101806.
- [23] Nesfchi, M.M., Pirbazari, A.E., Saraei, F.E.K., Rojaee, F., Mahdavi, F., Faal Rastegar, S.A., Fabrication of plasmonic nanoparticles/cobalt doped TiO₂ nanosheets for degradation of tetracycline and modeling the process by artificial intelligence techniques, *Materials Science in Semiconductor Processing*, 122, 2021, 105465.
- [24] Hosseinzadeh, A., Zhou, J.L., Altaee, A., Baziar, M., Li, X., Modeling water flux in osmotic membrane bioreactor by adaptive network-based fuzzy inference system and artificial neural network, *Bioresour. Technology*, 310, 2020, 123391.
- [25] Hernández-Julio, Y.F., Prieto-Guevara, M.J., Nieto-Bernal, W., Fuzzy clustering and dynamic tables for knowledge discovery and decision-making: Analysis of the reproductive performance of the marine copepod *Cyclopina* sp, *Aquaculture*, 523, 2020, 735183.
- [26] Ghobadi, M., Zaarei, D., Naderi, R., Asadi, N., Seyedi, S.R., Avard, M.R., Improvement the protection performance of lanolin based temporary coating using benzotriazole and cerium (III) nitrate: Combined experimental and computational analysis, *Progress in Organic Coatings*, 151, 2021, 106085.
- [27] Xu, Y., Zhu, Y., Xiao, G., Ma, C., Application of artificial neural networks to predict corrosion behavior of Ni-SiC composite coatings deposited by ultrasonic electrodeposition, *Ceramics International*, 40(4), 2014, 5425-5430.
- [28] Gan, H., Liu, G., Shi, C., Tang, R., Xiong, Y., Liu, Y., Liu, H., Comparison of three artificial neural networks for predict the electrodeposition of nano-silver film, *Materials Today Communications*, 26, 2021, 101950.
- [29] Li, X., Zhu, Y., Xiao, G., Application of artificial neural networks to predict sliding wear resistance of Ni-TiN nanocomposite coatings deposited by pulse electrodeposition, *Ceramics International*, 40(8), 2014, 11767-11772.
- [30] Yaghoot-Nezhad, A., Moradi, M., Rostami, M., Danaee, I., Khosravi-Nikou, M.R., Dual Z-Scheme CuO-ZnO@ Graphitic Carbon Nitride Ternary Nanocomposite with Improved Visible Light-Induced Catalytic Activity for Ultrasound-Assisted Photocatalytic Desulfurization, *Energy & Fuels*, 34(11), 2020, 13588-13605.
- [31] Moradi, M., Hasanvandian, F., Isari, A.A., Hayati, F., Kakavandi, B., Setayesh, S.R., CuO and ZnO co-anchored on g-C₃N₄ nanosheets as an affordable double Z-scheme nanocomposite for photocatalytic decontamination of amoxicillin, *Applied Catalysis B: Environmental*, 285, 2021, 119838.
- [32] Franco, D.S., Duarte, F.A., Salau, N.P.G., Dotto, G.L., Analysis of indium (III) adsorption from leachates of LCD screens using artificial neural networks (ANN) and adaptive neuro-fuzzy inference systems (ANIFS), *Journal of Hazardous Materials*, 384, 2020, 121137.
- [33] Zhou, Q., Wang, F., Zhu, F., Estimation of compressive strength of hollow concrete masonry prisms using artificial neural networks and adaptive neuro-fuzzy inference systems, *Construction and Building Materials*, 125, 2016, 417-426.
- [34] Xu, J., Zhao, X., Yu, Y., Xie, T., Yang, G., Xue, J., Parametric sensitivity analysis and modelling of mechanical properties of normal-and high-strength recycled aggregate concrete using grey theory, multiple nonlinear regression and artificial neural networks, *Construction and Building Materials*, 211, 2019, 479-491.
- [35] Reddy, N.S., Krishnaiah, J., Hong, S.G., Lee, J.S., Modeling medium carbon steels by using artificial neural networks, *Materials Science and Engineering: A*, 508(1-2), 2009, 93-105.
- [36] Gupta, T., Patel, K.A., Siddique, S., Sharma, R.K., Chaudhary, S., Prediction of mechanical properties of rubberised concrete exposed to elevated temperature using ANN, *Measurement*, 147, 2019, 106870.
- [37] Sugeno, M., Kang, G.T., Structure identification of fuzzy model, *Fuzzy Sets and Systems*, 28(1), 1998, 15-33.
- [38] Jang, J.S., ANFIS: adaptive-network-based fuzzy inference system, *IEEE Transactions on Systems, Man, and Cybernetics*, 23(3), 1993, 665-685.
- [39] Gerek, I.H., House selling price assessment using two different adaptive neuro-fuzzy techniques, *Automation in Construction*, 41, 2014, 33-39.
- [40] Abadi, S.N.R., Mehrabi, M., Meyer, J.P., Prediction and optimization of condensation heat transfer coefficients and pressure drop of R134a inside an inclined smooth tube, *International Journal of Heat and Mass Transfer*, 124, 2018, 953-966.
- [41] Hasanvandian, F., Moradi, M., Samani, S.A., Kakavandi, B., Setayesh, S.R., Noorisepehr, M., Effective promotion of g-C₃N₄ photocatalytic performance via surface oxygen vacancy and coupling with bismuth-based semiconductors towards antibiotics degradation, *Chemosphere*, 287, 2022, 132273.
- [42] Xu, J.H., Ye, S., Di Ding, C., Tan, L.H., Fu, J.J., Autonomous self-healing supramolecular elastomer reinforced and toughened by graphitic carbon nitride nanosheets tailored for smart anticorrosion coating application, *Journal of Materials Chemistry A*, 6(14), 2018, 5887-5898.
- [43] Li, C., Cao, C.B., Zhu, H.S., Graphitic carbon nitride thin films deposited by electrodeposition, *Materials Letters*, 58(12-13), 2004, 1903-1906.
- [44] Bai, X., Zong, R., Li, C., Liu, D., Liu, Y., Zhu, Y., Enhancement of visible photocatalytic activity via Ag@ C₃N₄ core-shell plasmonic composite, *Applied Catalysis B: Environmental*, 147, 2014, 82-91.
- [45] Benea, L., Danaila, E., Celis, J.P., Influence of electro-co-deposition parameters on nano-TiO₂ inclusion into nickel matrix and properties characterization of nanocomposite coatings obtained, *Materials Science and Engineering: A*, 610, 2014, 106-115.
- [46] Yasin, G., Khan, M.A., Arif, M., Shakeel, M., Hassan, T.M., Khan, W.Q., Zuo, Y., Synthesis of spheres-like Ni/graphene nanocomposite as an efficient anti-corrosive coating: effect of graphene content on its morphology and mechanical properties, *Journal of Alloys and Compounds*, 755, 2018, 79-88.
- [47] Beltowska-Lehman, E., Bigos, A., Indyka, P., Chojnacka, A., Drewienkiewicz, A., Zimowski, S., Szczerba, M.J., Optimisation of the electrodeposition process of Ni-W/ZrO₂ nanocomposites, *Journal of Electroanalytical Chemistry*, 813, 2018, 39-51.
- [48] Rasooli, A., Safavi, M.S., Babaei, F., Ansarian, A., Electrodeposited Ni-Fe-Cr₂O₃ nanocomposite coatings: A survey of influences of Cr₂O₃ nanoparticles loadings in the electrolyte, *Journal of Alloys and Compounds*, 822, 2020, 153725.
- [49] Demir, M., Kanca, E., Karahan, I.H., Characterization of electrodeposited Ni-Cr/hBN composite coatings, *Journal of Alloys and Compounds*, 844, 2020, 155511.
- [50] Ogihara, H., Wang, H., Saji, T., Electrodeposition of Ni-B/SiC composite films with high hardness and wear resistance, *Applied Surface Science*, 296, 2014, 108-113.
- [51] Li, B., Zhang, W., Huan, Y., Dong, J., Synthesis and characterization of Ni-B/Al₂O₃ nanocomposite coating by electrodeposition using trimethylamine borane as boron precursor, *Surface and Coatings Technology*, 337, 2018, 186-197.
- [52] Zhao, K., Shen, L., Qiu, M., Tian, Z., Jiang, W., Preparation and properties of nanocomposite coatings by pulsed current-jet electrodeposition, *International Journal of Electrochemical Science*, 12, 2017, 8578-8590.
- [53] Maharana, H.S., Mondal, K., Manifestation of Hall-Petch breakdown in nanocrystalline electrodeposited Ni-MoS₂ coating and its structure dependent wear resistance behavior, *Surface and Coatings Technology*, 2021, 410, 126950.
- [54] Xue, Z., Lei, W., Wang, Y., Qian, H., Li, Q., Effect of pulse duty cycle on mechanical properties and microstructure of nickel-graphene composite





- coating produced by pulse electrodeposition under supercritical carbon dioxide, *Surface and Coatings Technology*, 325, 2017, 417-428.
- [55] Smith, G.N., *Probability and statistics in civil engineering*, Collins Professional and Technical Books, 244, 1986.
- [56] Gandomi, A.H., Mohammadzadeh, D., Pérez-Ordóñez, J.L., Alavi, A.H., Linear genetic programming for shear strength prediction of reinforced concrete beams without stirrups, *Applied Soft Computing*, 19, 2014, 112-120.
- [57] Roy, P.P., Roy, K., On some aspects of variable selection for partial least squares regression models, *QSAR & Combinatorial Science*, 27(3), 2008, 302-313.
- [58] Tavana, M., Fallahpour, A., Di Caprio, D., Santos-Arteaga, F.J., A hybrid intelligent fuzzy predictive model with simulation for supplier evaluation and selection, *Expert Systems with Applications*, 61, 2016, 129-144.
- [59] Vellaichamy, B., Periakaruppan, P., Catalytic hydrogenation performance of an in situ assembled Au@g-C₃N₄-PANI nanoblend: synergistic inter-constituent interactions boost the catalysis, *New Journal of Chemistry*, 41(15), 2017, 7123-7132.
- [60] Liu, L., Qi, Y., Lu, J., Lin, S., An, W., Liang, Y., Cui, W., A stable Ag₃PO₄@ g-C₃N₄ hybrid core@ shell composite with enhanced visible light photocatalytic degradation, *Applied Catalysis B: Environmental*, 183, 2016, 133-141.
- [61] Komatsu, T., The first synthesis and characterization of cyameluric high polymers, *Macromolecular Chemistry and Physics*, 202, 2001, 19-25.
- [62] Giannakopoulou, T., Papailias, I., Todorova, N., Boukos, N., Liu Y., Yu, J., Trapalis C., Tailoring the energy band gap and edges' potentials of g-C₃N₄/TiO₂ composite photocatalysts for NO_x removal, *Chemical Engineering Journal*, 310, 2017, 571-580.
- [63] Aal, A.A., Gobran, H.A., Muecklich, F., Electrodeposition of Ni-RuAl composite coating on steel surface, *Journal of Alloys and Compounds*, 473(1-2), 2009, 250-254.
- [64] Khalaj, O., Ghobadi, M., Saebnoori, E., Zarezadeh, A., Shishesaz, M., Mašek, B., Štadler, C., Svoboda, J., Development of Machine Learning Models to Evaluate the Toughness of OPH Alloys, *Materials*, 14(21), 2021, 6713.

ORCID iD

Alireza Zarezadeh  <https://orcid.org/0000-0002-6581-9100>

Mohammad Reza Shishesaz  <https://orcid.org/0000-0001-6350-5215>

Mehdi Ravanavard  <https://orcid.org/0000-0002-6488-4146>

Moslem Ghobadi  <https://orcid.org/0000-0003-0474-8828>

Farzaneh Zareipour  <https://orcid.org/0000-0001-6017-0560>

Mohammad Mahdavian  <https://orcid.org/0000-0001-8470-6833>



© 2022 Shahid Chamran University of Ahvaz, Ahvaz, Iran. This article is an open access article distributed under the terms and conditions of the Creative Commons Attribution-NonCommercial 4.0 International (CC BY-NC 4.0 license) (<http://creativecommons.org/licenses/by-nc/4.0/>).

How to cite this article: Zarezadeh A., Shishesaz M.R., Ravanavard M., Ghobadi M., Zareipour F., Mahdavian M. Electrochemical and Mechanical Properties of Ni/g-C₃N₄ Nanocomposite Coatings with Enhanced Corrosion Protective Properties: A Case Study for Modeling the Corrosion Resistance by ANN and ANFIS Models, *J. Appl. Comput. Mech.*, 9(3), 2023, 590-606. <https://doi.org/10.22055/JACM.2021.38403.3220>

Publisher's Note Shahid Chamran University of Ahvaz remains neutral with regard to jurisdictional claims in published maps and institutional affiliations.

